# Microscale packed bed reactor for controlled hydrogen peroxide decomposition as a fuel cell oxidant aboard unmanned undersea vehicles

E. Lennon [a,*], A.A. Burke [b], M. Ocampo [a], R.S. Besser [a]

[a] Department of Chemical Engineering and Materials Science, Stevens Institute of Technology, Castle Point on Hudson, Hoboken, NJ 07030, United States
[b] Naval Undersea Warfare Center, Newport, RI 02841, United States

## ARTICLE INFO

## ABSTRACT

The multiphase catalytic decomposition of hydrogen peroxide into water and oxygen is notoriously susceptible to thermal runaway (heat of reaction: $-98 \, \text{kJ mol}^{-1}$). The high surface area to volume ratio ($S/V$) in a microscale packed bed (MPB) reactor (radius 0.5 mm) was investigated for reducing the risk of thermal runaway during hydrogen peroxide decomposition to oxygen intended as a fuel cell oxidant aboard an unmanned undersea vehicle (UUV). A microscale reactor channel with a $S/V$ of $\sim 2 \times 10^3 \, \text{m}^2 \, \text{m}^{-3}$ simulated under convective cooling generated a significant heat rise ($T$ rise $\sim 100 \, \text{K}$), whereas a microreactor with a higher $S/V$ ($\sim 200 \times 10^3 \, \text{m}^2 \, \text{m}^{-3}$) achieved thermal control ($T$ rise $< 10 \, \text{K}$) over the simulated reaction zone. Although thermal management was successfully accomplished using the higher $S/V$, experimental conversions of hydrogen peroxide to oxygen (5–18%) measured from the outlet were lower than simulated conversions (38–63%). Simulation assumptions, such as homogeneously dispersed flow and perfect catalyst interaction among other factors, contributed to the discrepancies between the simulated and experimental degrees of peroxide conversion to oxygen. Even though thermal control of the MPB was achieved, this work indicates that mass transfer limitations are a factor in the MPB reactor during a multiphase reaction, like decomposition of hydrogen peroxide to oxygen and water, and suggests means to overcome them even on the microscale level.

© 2009 Elsevier B.V. All rights reserved.

## 1. Introduction

A major challenge facing the design of air-independent power systems is energy storage. High energy density and potentially low operating costs make fuel cells an attractive option for unmanned undersea vehicle (UUV) applications [1,2]. Modeling of an air-independent solid oxide fuel cell (SOFC) power system for UUVs by Burke and Carreiro showed that an efficiency of 45% is theoretically possible based on a 2.5 kW net output over 40 h [3]. To compete with current battery technologies, fuel cell systems like the UUV SOFC must also exceed 300 Wh L$^{-1}$, underscoring an inherent volume limitation associated with UUV power generation [4]. Additionally, air-independent fuel cell power systems require an oxidant supply. The work presented herein focused on supplying oxygen via hydrogen peroxide (H$_2$O$_2$) decomposition and evaluating the capabilities and limitations of such a microreactor used to provide oxygen. It is estimated that for a 2.5 kW net power output, a minimum total flow rate of 0.6 O$_2$ mol min$^{-1}$ (14.7 O$_2$ L min$^{-1}$) is required [3].

H$_2$O$_2$ readily decomposes into water (H$_2$O) and oxygen (O$_2$) via the reaction H$_2$O$_{2(l)} \rightarrow$ H$_2$O$_{(l)} + 1/2$O$_{2(g)}$ upon contact with a number of commercially available metal catalysts [5] offering a dense source of O$_2$ per unit volume. The availability of high O$_2$ density in a 60% (w/w) H$_2$O$_2$ solution facilitates ease of handling and makes concentrated H$_2$O$_2$ a valuable commodity as an air-independent fuel cell oxidant. Furthermore, the existing commercial infrastructure of H$_2$O$_2$ has long added to its appeal as an oxidant source [6]. Kinetic experiments have shown that manganese dioxide (MnO$_2$) is a relatively inexpensive, yet effective H$_2$O$_2$ decomposition catalyst with reported activation energies ranging from 20 to 44 kJ mol$^{-1}$ and was selected as the primary catalyst for this work [5,7–10]. Despite these advantages, it is well established that catalytic H$_2$O$_2$ decomposition is highly exothermic ($\Delta H^{\circ}_{\text{rxn}} = -98 \, \text{kJ mol}^{-1}$) [11]. This factor has historically limited its application as a power system oxidant, especially within the U.S. Navy community [12]. In addition, like other exothermic multiphase reactions, the liquid and gas product stream from H$_2$O$_2$ decomposition can lead to undesirable pressure increases, irregular distribution of thermal capacity in conventionally sized reactors, and the possibility of thermal runaway [13].

Microscale reactors, possessing relevant fluid dimension in subunits < 1 mm, have high surface to volume ratios ($S/V$) resulting in heat and mass transfer coefficients capable of inhibiting thermal

runaway. Conventional reactors with a relevant flow geometry of 10 cm, for example, have $S/V$s of $\sim 10\,\mathrm{m^2\,m^{-3}}$, whereas microscale reactors possess $S/V$s that are at least two orders of magnitude greater [14]. The microscale packed bed (MPB) reactor used in this work included an extended heat exchange surface and had a $S/V$ of $1.88 \times 10^5\,\mathrm{m^2\,m^{-3}}$. The small characteristic dimensions of microreactor subunits generally result in low Reynolds numbers and subsequently laminar flow [15]. Laminar flow minimizes irregularities and stabilizes flow in the reaction zone. Although laminar flow is typical in many homogenously dispersed product streams within microchannels, slug flow can also develop in multiphase flow scenarios [16]. In a study of microchemical decomposition of $H_2O_2$, two-phase flow evolution of $O_2$ gas bubbles and liquid water from platinum- catalyzed $H_2O_2$ decomposition in 80-$\mu$m diameter microchannels occurred in three different stages: liquid decomposition, bubble coalescence, and bubble slugs [16]. Despite the complexities of the multiphase product stream generated from $H_2O_2$ decomposition, in the present investigation we aimed to demonstrate thermal management feasibility and assess $O_2$ production during the catalytic multiphase decomposition of $H_2O_2$ using the MPB reactor.

## 2. Methods

### 2.1. MPB geometry

The semicircular MPB channel was 0.5 mm deep and 5 cm long. The MPB channel was embedded in a rectangular stainless steel 316 block ($7\,\mathrm{cm} \times 2\,\mathrm{cm} \times 0.4\,\mathrm{cm}$) which acted as the extended surface area. A Plexiglas (PMMA) cover ($7\,\mathrm{cm} \times 2\,\mathrm{cm} \times 0.1\,\mathrm{cm}$) sealed the top of the channel. Fig. 1 shows the dimensions of both the simulated MPB geometry (Fig. 1A) and the experimental MPB geometry (Fig. 1B).

The experimental reactor differed from the simulated MPB geometry slightly in that the inlets and outlets were positioned differently. In the experimental MPB, both the inlet and outlet were 1 cm from the MPB edges. The inlet of the simulated reactor microchannel was 2 cm from the edge of the MPB stainless steel block and the outlet of the simulated reactor microchannel was flush with the MPB edge. Shifting the simulated microchannel, so the outlet in the model was flushed with the external side surface, eliminated the need for a 90° angle which would have directed the microchannel towards the bottom external surface. This approach mi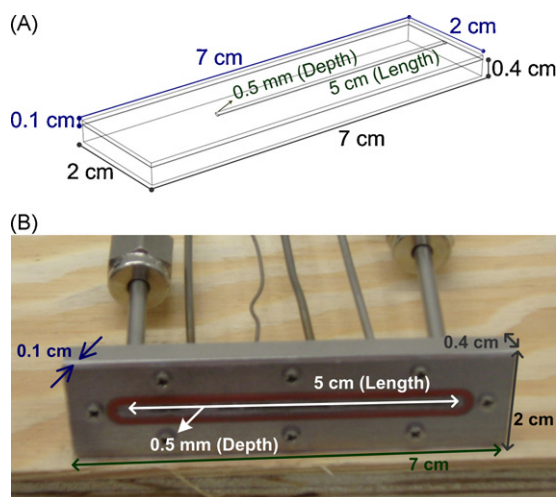nimized meshing issues and facilitated model convergence necessary for simulation of the three-dimensional temperature and concentration profiles. The meshing algorithm used during simulation created a mesh of over 17,000 tetrahedral finite elements, which was finer in the microchannel region where the reaction was defined.

### 2.2. Simulated $H_2O_2$ decomposition

#### 2.2.1. Governing equations and assumptions

A variety of multiphase flow regimes, such as homogeneously dispersed gas in liquid or intermittent slugs of gas and liquid, are capable of developing in microchannels. The evolving flow depends on a multitude of initial and dynamic flow conditions. Based on the operation of the decomposition reactor at atmospheric pressure and a temperature range from approximately 290 K to 330 K, it was not possible to determine *a priori* the flow regime or regimes that would evolve in the reactor, nor was the modeling algorithm able to make this prediction [17]. Consequently, when solving the governing equations for the reactor performing the multiphase $H_2O_2$ decomposition, we chose to describe the properties of the materials in the system as mass-weighted averages of properties of the phases present. For example, the density of the fluid within the control volume of the reactor was treated as a single homogeneous phase whose density is the weighted average of the density of the gas phase and the density of the liquid phase within the control volume [18].

*Mass balance.* $H_2O_2$ in the vapor phase was considered negligible based on the fact that equilibrium vapor concentration of 50% (w/w) $H_2O_2$ reactant (the highest nominal concentration used in this research) at 303 K is less than 6% [19]. Additionally, the amount of dissolved $O_2$ in the liquid was considered negligible compared to the $H_2O_2$ and water liquid components. Similarly, the amount of water vapor in the gas phase was considered negligible compared to the $O_2$ gas, provided the temperature remained below the boiling point of water (373 K). The mass balance included the effects of diffusion of $H_2O_2$ in a water–$H_2O_2$ mixture, the bulk flow of the evolving fluid mixture (consisting primarily of liquid $H_2O_2$ solution in water, and $O_2$ gas) down the reactor channel, and consumption of $H_2O_2$ resulting from the decomposition reaction. Eq. (1) governed the steady-state mass balance of $H_2O_2$.

$$-D_{\mathrm{H_2O_2\,eff}}\frac{\partial^2 C_{\mathrm{H_2O_2}}}{\partial x^2} - D_{\mathrm{H_2O_2\,eff}}\frac{\partial^2 C_{\mathrm{H_2O_2}}}{\partial y^2} - D_{\mathrm{H_2O_2\,eff}}\frac{\partial^2 C_{\mathrm{H_2O_2}}}{\partial z^2}$$
$$+ v_x \frac{\partial C_{\mathrm{H_2O_2}}}{\partial x} = r_{\mathrm{H_2O_2}} \qquad (1)$$

In Eq. (1), $D_{\mathrm{H_2O_2\,eff}}$ was the effective diffusivity of $H_2O_2$ in the water–$H_2O_2$ solution. The catalytic reaction rate law, $r_{\mathrm{H_2O_2}}$, served wholly as the conversion mechanism. The mass, energy (Eq. (2)), and momentum balances (Eq. (3)) were solved simultaneously for the $H_2O_2$ concentration ($C_{\mathrm{H_2O_2}}$), temperature ($T$), and velocity field ($U$) respectively using COMSOL Multiphysics 3.4. The variable $v_x$ represented the superficial velocity of the fluid in the $x$-axis direction. The rate of reaction, $r_{\mathrm{H_2O_2}}$, was established assuming first order kinetics weighted via an inputted catalyst mass [7]. A conventional Arrhenius relationship estimated during kinetic experiments with the MnO$_2$ catalyst defined the reaction rate constant coupling the mass balance to the energy balance (Eq. (2)). Appendices A and B entitled "Simulation Constants" and "Simulation Expressions" specify all values and expressions used in the models. All parameters were in SI units.

*Energy balance.* The energy balance included conduction, advective input and output due to the feed and exit streams, exothermic heat generation due to reaction, sensible heat, and the heat of water



**Fig. 1.** Microscale packed bed (MPB) reactor geometry used during simulation (A) and experimentation (B).

vaporization. Eq. (2) governed the steady-state energy balance.

$$-K_{eff}\frac{\partial^2 T}{\partial x^2} - K_{eff}\frac{\partial^2 T}{\partial y^2} - K_{eff}\frac{\partial^2 T}{\partial z^2} + v_x \rho c_p \frac{\partial T}{\partial x} = \Delta H_{rxn} r_{H_2O_2}$$
$$- S_h - \Delta H_{vap} r_{H_2O} \tag{2}$$

*Momentum balance.* The momentum balance was modeled as a steady-state, non-isothermal flow using the Navier–Stokes equations for weakly compressible flows, i.e., flows with Mach numbers < 0.3 [20]. Gravity forces were neglected. Eq. (3) governed the momentum balance, which is a reduced form of the Navier–Stokes equation under steady-state conditions.

$$\rho(U \cdot \nabla U) = -\nabla p + \eta \nabla^2 U \tag{3}$$

The first term in Eq. (3), referred to as "convective acceleration," is based on the position derivative of the velocity field which is independent of time [21]. The third term describes the effect of $\eta$, the fluid viscosity, on the velocity field. During laminar flow in the $x$-axis direction, the transverse components of the velocity are essentially negligible and Eq. (3) simplifies to Eq. (3a).

$$\rho\left(v_x \frac{\partial v_x}{\partial x}\right) = -\nabla p + \eta\left(\frac{\partial^2 v_x}{\partial x^2} + \frac{\partial^2 v_x}{\partial y^2} + \frac{\partial^2 v_x}{\partial z^2}\right) \tag{3a}$$

Eq. (4) is the continuity equation. Using low initial volumetric flow rates ranging from 0.05 ml min$^{-1}$ to 0.15 ml min$^{-1}$ (corresponding initial fluid velocities of 2.12–6.37 mm s$^{-1}$) maintained the conditions defining weakly compressible laminar fluid flow.

$$\nabla \cdot (\rho U) = 0 \tag{4}$$

The density, $\rho$, was modeled as an average of the liquid and gas comprising the fluid weighted by the mole fractions of $H_2O_2$, $H_2O$, and $O_2$ species respectively and changed as the reaction progressed (Eq. (5)). This average density was applied under the simplifying assumption that the generated $O_2$ gas was homogenously dispersed throughout the fluid and the effluent stream maintained a well-mixed, dispersed phase.

$$\rho = x_{H_2O_2}\rho_{H_2O_2} + x_{H_2O}\rho_{H_2O} + y_{O_2}\rho_{O_2} \tag{5}$$

### 2.2.2. Boundary conditions

For the inlet boundary condition of the mass balance, the $H_2O_2$ concentration was set equal to the feed concentration. The outlet boundary condition of the mass flux was defined as purely convective, since after leaving the reactive environment no diffusive effects occur. The microchannel reactor walls constrain the total normal mass flux to zero.

For the inlet boundary condition of the energy balance, the fluid temperature was set equal to the initial fluid temperature. The fluidic outlet boundary condition of the energy flux was defined as purely convective, since the reactor ends at that point and any connecting tubing would have negligible conductive losses relative to the main MPB reactor unit. To simulate convective cooling under ambient conditions in air, external heat flux defined the boundary condition imposed on all external surfaces exposed to the surrounding environment. At the outer-wall, air interface, which occurs at the external surfaces exposed to the ambient environment, natural convection is the limiting aspect of the dissipation of heat produced from the reactor unit. Continuity of both the convective and conductive heat fluxes defined the boundaries of the internal surfaces of the microchannel embedded in the stainless steel block and underneath the Plexiglas cover for the energy balance.

In the momentum balance the superficial velocity was set equal to the initial superficial velocity in the $x$-direction at the inlet. No slip was assumed at the MPB reactor walls, and at that boundary the

fluid velocity was set equal to zero. The outlet boundary condition for the momentum balance was defined by normal pressure and flow. Appendix C summarizes the simulated boundary conditions.

### 2.3. Experimental $H_2O_2$ decomposition

*Setup and data collection.* Effluent $O_2$ gas rates and temperature data from the physical reactor were collected using the setup shown in Fig. 2. A World Precision Instruments SP2001 syringe pump dispensed nominal 50% weight in water (measured 55%, w/w) $H_2O_2$ supplied by Sigma–Aldrich at volumetric flow rates (VFR) 0.05 ml min$^{-1}$ (8.3 × 10$^{-10}$ m$^3$ s$^{-1}$) and 0.15 ml min$^{-1}$ (2.5 × 10$^{-9}$ m$^3$ s$^{-1}$). These volumetric flow rates correspond to initial reactant velocities of 2.12 mm s$^{-1}$ and 6.37 mm s$^{-1}$, respectively. Two type J and two type K thermocouples were placed in 10 mm increments down the length of the MPB reactor channel. A National Instruments USB 9211 digital to analog converter connected to 9162 USB data acquisition device transmitted the temperature data to the computer for temperature data collection and storage. The effluent multiphase product stream consisting primarily of liquid $H_2O_2$ and $H_2O$ and gaseous $O_2$ flowed from the MPB reactor to the liquid collection vial. The $O_2$ gas proceeded to an Aalborg oxygen flow meter. A National Instruments USB 6008 digital-to-analog converter transmitted the flow data to the laptop for collection and storage. The program Labview Signal Express controlled both the temperature and flow data recording processes. At the end of each experimental run, standard potassium permanganate ($KMnO_4$) titrations were conducted with the liquid solution collected from the MPB outlet in the sample vial to determine the steady-state outlet concentration of $H_2O_2$ and conversion [22].

*MPB reactor preparation.* The results of the MPB modeling efforts were used as the basis of the MPB design completed in a CAD program. The experimental MPB reactor was fabricated at a precision machine shop using type 316 stainless steel. Glass wool was plugged at the inlet and outlet to keep catalyst within the reactor microchannel. $MnO_2$ catalyst (Mallinckrodt Baker: product codes 5308, 8329) with particles ranging in diameter from 60 to 110 μm and an average particle diameter of 75 μm was applied to the MPB reaction channel. The reaction rate constant per catalyst mass was estimated during kinetic experiments with the $MnO_2$ catalyst particles and provided the values of the activation energy and frequency factor used in the FEM model. The differential reactor mass was recorded and gave the $MnO_2$ catalyst mass, which was 0.014 ± 0.002 g for all experiments.

## 3. Results and discussion

### 3.1. Simulated MPB

Fixing the height of the simulated reactor channel to 0.5 mm and varying its length, a length of 5 cm yielded 42% conversion at the outlet using 50% (w/w) $H_2O_2$ reactant and an initial volumetric flow rate of 0.15 ml min$^{-1}$ (initial fluid velocity of 6.37 mm s$^{-1}$). However, a temperature rise of 92 K was simulated across the microchannel reactor lacking the extended surface area as shown in Fig. 3. Despite microscale geometry ($S/V$ of 2.3 × 10$^3$ m$^2$ m$^{-3}$) the simulated reactor channel without extended surface area failed to prevent significant heat rise. An outlet temperature exceeding 373 K would lead to unwanted water vaporization in the effluent stream and subsequently increased pressure, both of which were outcomes beyond the scope of the simulation assumptions. This finding reinforced the inherent risk of thermal runaway and other possible thermal effects due to the exothermic nature of the $H_2O_2$ decomposition reaction.
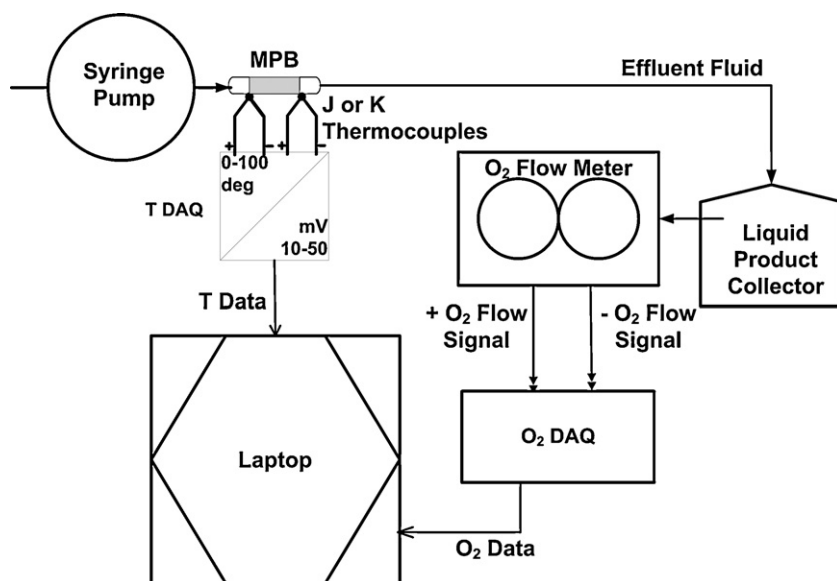
**Fig. 2.** Experimental setup used during $H_2O_2$ decomposition with the MPB reactor.

Consequently the surface area surrounding the simulated reactor channel was extended to improve passive cooling of the simulated MPB reactor by increasing the $S/V$. The final simulated MPB reactor geometry included the stainless steel block of the dimensions displayed in Fig. 1A and had a $S/V$ of $188 \times 10^3$ m$^2$ m$^{-3}$, approximately two orders of magnitude larger than the original microchannel $S/V$. Fig. 3 also shows the resulting steady-state temperature (K) and $H_2O_2$ concentration (mol m$^{-3}$) profiles down the length of the simulated reactor channel with an extended surface area. The temperature rise down the length of the simulated reactor channel surrounded by the extended surface area was only 7 K with an outlet temperature of 299 K. The extended surface area significantly enhanced thermal control of the simulated reaction zone and ensured the outlet temperature remained well below the boiling point of water (373 K) while achieving a conversion of 38% calculated 0.25 mm from the reactor wall.

The outlet temperature variation in the radial direction ranged from an average of 299.53 K to a maximum of 299.75 K, and was insignificant compared to the change in the axial direction. The outlet $H_2O_2$ concentration in the radial direction ranged from an average of 10,852 mol m$^{-3}$ to a minimum of 6283 mol m$^{-3}$. The concentration variation over the outlet resulted from decreasing

velocity of the fluid towards the rector wall and subsequently greater residence times. There is slightly more conversion of hydrogen peroxide at the outlet of the simulated MPB reactor without extended surface area because of the additional thermal energy available to promote the reaction.

Simulations were run at lower initial volumetric flow rates using the MPB geometry including the extended surface area for improved heat exchange. Initial volumetric flow rates lower than 0.15 ml min$^{-1}$ (initial fluid velocity of 6.37 mm s$^{-1}$) also exhibited thermal control over the simulated reaction zone by limiting the release of reaction heat. Fig. 4 shows the simulation results of the three-dimensional finite element MPB model using an initial 50% $H_2O_2$ reactant and volumetric flow rate of 0.05 ml min$^{-1}$ (initial fluid velocity of 2.12 mm s$^{-1}$), the minimum flow rate used in this study.

A corresponding temperature rise over the MPB reactor of 5 K and a conversion of 63% calculated 0.25 mm from the reactor wall were obtained. The outlet temperature variation in the radial direction ranged from an average of 297.72 K to a maximum of 297.90 K. The outlet $H_2O_2$ concentration in the radial direction ranged from an average of 6505 mol m$^{-3}$ to a minimum of 3371 mol m$^{-3}$. The lower reactant volumetric flow rate effectively increased residence time in the reactor channel in the axial direction causing greater conversion per unit volume of reactant. In addition to increased conversion, there was also decreased temperature rise due to the lower processing rate. For the simulated conversion of 63% at the minimum 0.05 ml min$^{-1}$ volumetric flow rate the corresponding oxygen flow rate was 5.8 ml min$^{-1}$ at the outlet. Despite the lower simulated conversion of 37% at the maximum 0.15 ml min$^{-1}$ volumetric flow rate, the corresponding oxygen flow rate would be 10.1 ml min$^{-1}$ at the outlet. Although the smaller volumetric flow rate resulted in higher conversion in conjunction with decreased temperature rise, the amount of total oxygen generated per unit time exiting the reactor is reduced at the lower reactant volumetric flow rate. Thus the simulations, which are based on source terms for the kinetic reaction expressions, presented an inherent trade-off between conversion efficiency and outlet oxygen flow rate dependent upon the initial reactant volumetric flow rate. A future parametric study of the MPB reactor is suggested to discover the optimum initial volumetric flow rate based on the oxygen flow rate requirement for the UUV fuel cell system.
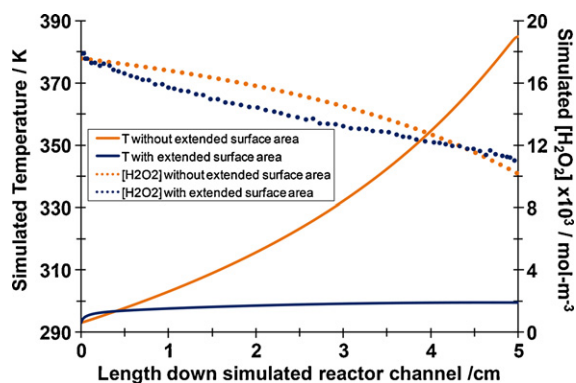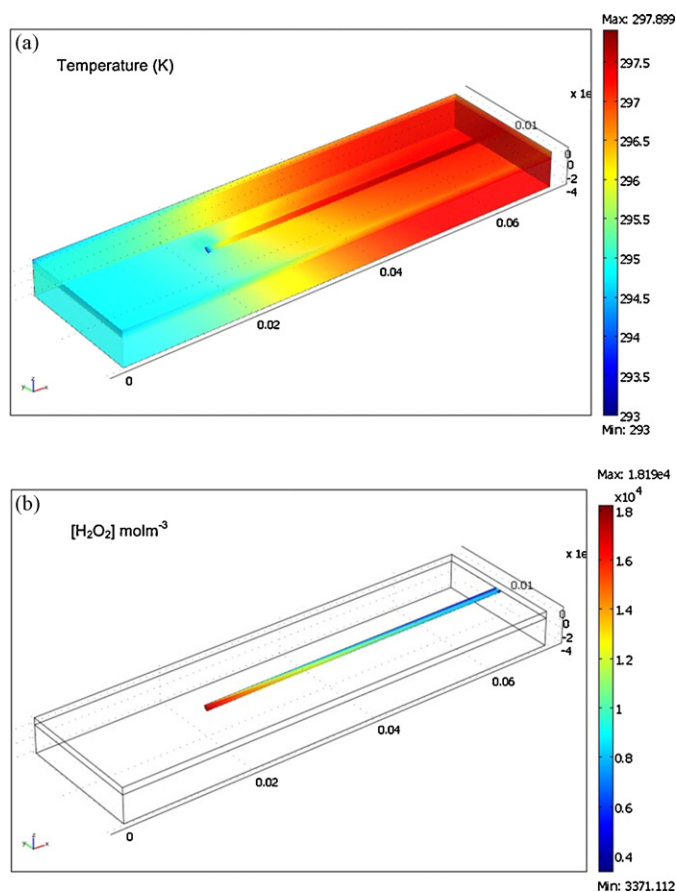


**Fig. 3.** Temperature in K and $H_2O_2$ concentration in mol m$^{-3}$ down the length of the simulated reactor channel using an initial reactant concentration of 50% $H_2O_2$ and volumetric flow rate of 0.15 ml min$^{-1}$ simulated with and without an extended surface area surrounding the reactor channel.

**Fig. 4.** Three-dimensional temperature distribution in K (top) and $H_2O_2$ concentration in mol m$^{-3}$ (bottom) of the simulated MPB run using an initial reactant concentration of 50% $H_2O_2$ and volumetric flow rate of 0.05 ml min$^{-1}$ and convection coefficient of 10 W m$^{-2}$ K$^{-1}$.

### 3.2. Experimental vs. simulated temperature

Using the temperature data collected from the experimental MPB, the experimental and simulated temperatures were compared. Fig. 5 gives the average experimental steady-state temperatures recorded at 10 mm increments down the length of the MPB reactor in comparison to the simulated steady-state temperature profiles given by the trend lines down the center length of the simulated MPB reactor using an initial 50% (w/w) $H_2O_2$ reactant at the minimum volumetric flow rate of 0.05 ml min$^{-1}$ (2.12 mm s$^{-1}$) and maximum volumetric flow rate of 0.15 ml min$^{-1}$ (6.37 mm s$^{-1}$).
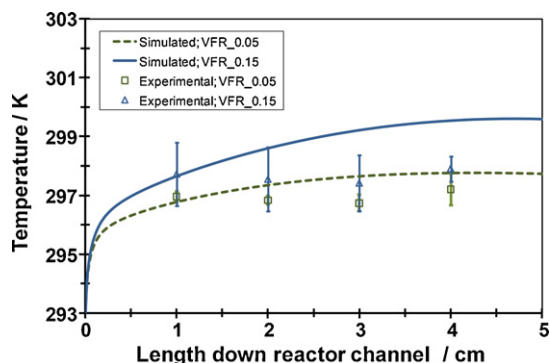


**Fig. 5.** Experimentally recorded and simulated steady-state MPB temperatures down the reactor length using initial 50% (w/w) $H_2O_2$ reactant with volumetric flow rates of 0.05 ml min$^{-1}$ and 0.15 ml min$^{-1}$.

The temperature rise was less than 7 K for both the simulated and experimental MPB confirming improved thermal control upon integration of the extended surface area.

Fig. 5 also shows that the experimental MPB readings were within a 2 K range of those simulated. Although the simulated and experimental MPB temperatures were similar, the increase in temperature approaching the MPB outlet at 5 cm seen during simulation was not replicated during experimentation. This discrepancy was partially due to uneven catalyst loading in the experimental MPB reactor which was exacerbated during the progression of the multiphase reaction. As the reaction progressed, the initially packed catalyst particles were dislodged and aggregated into irregularly distributed catalyst regions. The experimental temperatures were lower than expected 3 cm down the reactor channel because a void in the catalyst packing was observed at that location. Two and four centimeter down the length of the MPB, larger clumps of catalyst aggregated and temperature recordings were correspondingly higher due to greater localized conversion. Higher temperatures were observed for both the simulated and experimental maximum volumetric flow rate as well. This was expected because there was more reactant available for conversion and correspondingly exothermic heat generation at the higher volumetric flow rate. The experimental temperatures were consistently lower than those simulated at both volumetric flow rates. The decrease in experimental MPB temperatures relative to the simulation under equivalent conditions was due to the lower experimental conversions.

### 3.3. Experimental vs. simulated conversion

Fig. 6 shows the experimental steady-state outlet conversions were lower than those simulated under equivalent conditions. Since the reactant dispensed at 0.05 ml min$^{-1}$ experienced greater residence time, it produced higher simulated (63%) and experimental (18%) conversions relative to the simulated (37%) and experimental (5%) conversions resulting from reactant dispensed at 0.15 ml min$^{-1}$. Lower experimental conversions resulted in the low effluent $O_2$ flow rates measured from the experimental MPB. When the syringe pump dispensed the 50% $H_2O_2$ reactant at 0.05 ml min$^{-1}$, the average experimentally measured effluent $O_2$ flow rate was 0.84 ml min$^{-1}$. When the syringe pump dispensed the 50% $H_2O_2$ reactant at 0.15 ml min$^{-1}$, the average experimentally measured effluent $O_2$ flow rate was 1.15 ml min$^{-1}$.

### 3.4. Factors reducing experimental conversion

In addition to unbalanced catalyst loading and an inherent propensity for particle aggregation during reaction in the experimental MPB reactor mentioned in Section 3.2, the development of $O_2$ gas bubbles at active catalyst sites likely reduced experimental
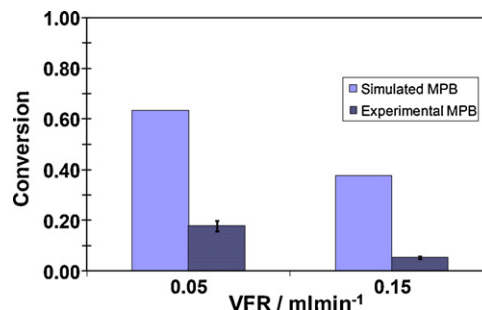


**Fig. 6.** Experimental and simulated steady-state outlet conversions using initial 50% (w/w) $H_2O_2$ reactant and volumetric flow rates (VFR) of 0.05 ml min$^{-1}$ and 0.15 ml min$^{-1}$.

conversion and overall experimental oxygen production. The observation of $O_2$ bubbles intermittently affixed to catalyst particles in the MPB microchannel supports the notion that active site blocking by $O_2$ gas bubbles caused lower conversion than expected. This mass transfer limitation effectively restricts continuous access of $H_2O_2$ reactant to active catalyst sites in turn decreasing conversion and subsequently oxygen production.

Observations of gas bubbles indicated deviation from the assumption of a homogenous, well-mixed effluent used during simulation. The presence of such gas slugs reduces contact time between the reactive stream and catalyst. This reduced contact time essentially results in a lower residence time and is likely to have contributed to the reduction in experimental conversion. This is indicative of one of the fundamental challenges of multiphase reactions taking place in microscale reactors.

Another factor influencing and likely suppressing experimental conversion and oxygen generation in comparison to those simulated under equivalent conditions is the type and quantity of stabilizer present in the 50% stock $H_2O_2$ reactant used. Fully characterizing the effect of $H_2O_2$ stabilizers is challenging because stabilizer information remains proprietary and varies among suppliers. Preliminary experimental runs with a stock of stabilized $H_2O_2$ resulted in decreased oxygen production over the course of an hour. Fig. 7 displays the experimental effluent oxygen flow rate measured from the MPB outlet versus time in minutes using the stabilized reactant. The decline in oxygen production is clear based on the trend line illustrated. Although stabilizers were present, the model is still informative especially in regard to understanding the thermal performance of the system which is the primary objective of the study. To more closely predict the conversion, the reaction rate law can be modified to capture the effect of the stabilizer [23], or simulation and experiments can be performed with alternate noble metal catalysts which are less susceptible to degradation from the stabilizers [24]. The effects of such proprietary stabilizers on decomposition catalysts must be more fully examined in future studies.

In addition to improved characterization of peroxide stabilizers, improved catalyst application techniques would be helpful in reducing the differences between simulated and experimental results as well as in enhancing overall oxygen production of the microreactor. For example, a thin layer that acts as an adherent for catalyst particles could be employed. Fig. 8 depicts the microscale reactor with a thin layer of adherent lining which keeps $MnO_2$ catalyst particles fixed to the inside wall of the channel. Using the adherent lining, which is a carbon ink compound the decomposi-
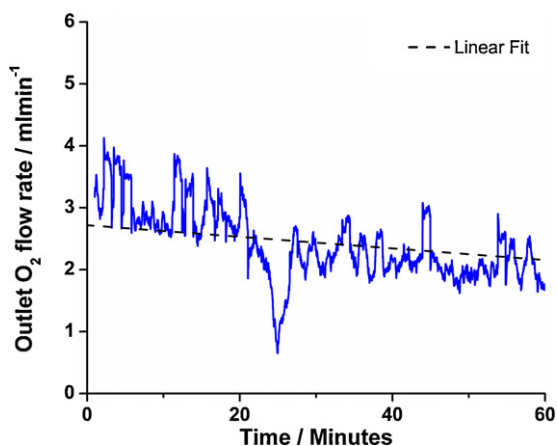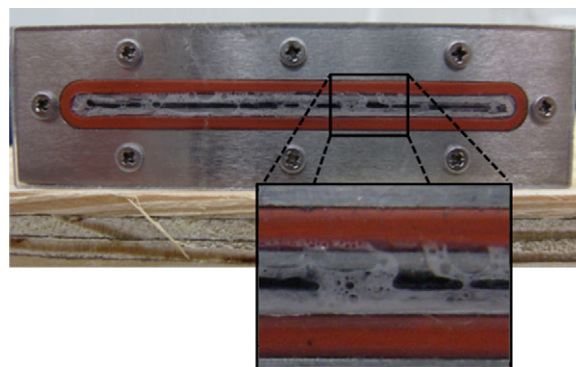


**Fig. 8.** Section of microscale reactor in which the black adherent lining, a carbon ink compound, is used to hold catalyst particles to the inside wall of the channel. The resulting effluent stream displays a well-mixed dispersed somewhat frothy phase in which the $O_2$ gas bubbles more readily mix with the liquid solution.

tion catalyst stays fixed along the wall of the microscale reaction channel. This approach not only deters clog formation but also seems to promote better dispersion of the $O_2$ gas in the liquid stream as the effluent appears more homogenous when the catalyst lines the wall of the reaction channel. The observation of a more readily dispersed fluid in the MPB may overcome some of the identified drawbacks to the packed catalyst approach, such as stubborn $O_2$ bubbles immobilized at active catalyst sites and blockages. The exploration of optimal catalyst application also remains a topic for future investigations.

## 4. Conclusions

With the advent of microchemical technology, there is a temptation to assume that even highly exothermic reactions can be made to proceed nearly isothermally simply by implementing microscale geometry [25]. However, the significant temperature rise in the simulated microchannel reactor without extended surface area emphasized that highly exothermic reactions are not necessarily near-isothermal even at sub-mm diameters. Increasing the $S/V$ ultimately achieved thermal control over the reaction zone. High area heat exchange surfaces, like the one added to the MPB reactor, offer an easily integrated, passive mechanism to mitigate the risk of thermal runaway in microscale reactors. Although simulations were shortcoming in capturing the behaviors exhibited in the experimental effluent, they indicated conversions greater than 30% would be possible under improved catalyst utilization.

To increase experimental oxygen production with the MPB, a continuous, even distribution of catalyst particles in the reactor microchannel is needed. Catalyst application along the reactor wall using an adherent thin layer is one alternative that deserves future investigation. This technique could offer more open volume in the microchannel and permit oxygen gas to be efficiently removed, rather than being trapped in the voids of the packed reactor, potentially overcoming the experimentally observed mass transfer limitations from the fixation of oxygen bubbles at active catalyst sites.

Since commercial $H_2O_2$ stabilizers likely contributed to catalyst deactivation of the $MnO_2$ catalyst in the work here, better characterization of stabilizers and their impact on the reactor's catalyst requires additional investigation. Although microscale reactor heat dissipation is easily improved passively, the MPB approach is subject to inherent mass transfer challenges that should be addressed via optimization of catalyst application and reactor geometry. Resolving these issues will facilitate the realization of a multi-unit microchemical system for greater total oxygen production levels.



**Fig. 7.** Decrease in experimental effluent oxygen flow rate in ml min$^{-1}$ over time using stabilized 50% $H_2O_2$ reactant with an initial volumetric flow rate of 0.15 ml min$^{-1}$.

These findings present a foundation for thermally controlled $H_2O_2$ decomposition microscale reactors and suggest mechanisms for further reactor optimization to achieve increased oxygen generation rates for UUV SOFC power systems.

## Acknowledgement

## Appendix A. Simulation constants

| Equation symbol | Values | Description | SI units |
|---|---|---|---|
| $v_o$ | $2 \times 10^{-11}$ to $2 \times 10^{-8}$ | Initial volumetric flow rate | $m^3\,s^{-1}$ |
| $v_{xo}$ | $5 \times 10^{-5}$ to $5 \times 10^{-2}$ | Initial superficial fluid velocity in $x$-direction | $m\,s^{-1}$ |
| $T_o$ | 293 | Initial temperature | K |
| $E_a$ | 20,400 | Reaction rate law activation energy | $J\,mol^{-1}$ |
| $A$ | 2,910 | Reaction rate law frequency factor | $mol\,m^{-3}\,s^{-1}\,g_{cat}^{-1}$ |
| $\rho_{H_2O_2}$ | 1097 | Average $H_2O_2$ density of solution in reactor | $kg\,m^{-3}$ |
| $\rho_{H_2O}$ | 998 | Density of water | $kg\,m^{-3}$ |
| $\rho_{O_2}$ | 1.3 | Average $O_2$ density between 273 and 350 K | $kg\,m^{-3}$ |
| $K_{eff}$ | 5.65 | Effective thermal conductivity of microchannel | $W\,m^{-1}\,K^{-1}$ |
| $T_{ambient}$ | 290 | Ambient temperature | K |
| $h_{conv}$ | 10 | Estimated natural convective heat flux for air | $W\,m^{-2}\,K^{-1}$ |
| $mw_p$ | 0.034 | Molecular weight of $H_2O_2$ | $kg\,mol^{-1}$ |
| $mw_{H_2O}$ | 0.018 | Molecular weight of $H_2O$ | $kg\,mol^{-1}$ |
| $\Delta H_{rxn}$ | 98,200 | Heat of reaction | $J\,mol^{-1}$ |
| $R$ | 8.314 | Ideal gas constant | $J\,mol^{-1}\,K^{-1}$ |
| $c_p$ | 3731 | Average $H_2O_2$ reactor solution heat capacity | $J\,kg^{-1}\,K^{-1}$ |
| $M_{cat}$ | 0.015–0.030 | Mass of catalyst | g |
| $D_{effpH_2O}$ | $7.85 \times 10^{-10}$ | Average effective diffusivity of $H_2O_2$ into water | $m^2\,s^{-1}$ |
| $D_{effpp}$ | $2.71 \times 10^{-12}$ | Average effective diffusivity of $H_2O_2$ into $H_2O_2$ | $m^2\,s^{-1}$ |
| $\rho_{ss}$ | 8000 | Density of stainless steel 316 | $kg\,m^{-3}$ |
| $c_{pss}$ | 500 | Heat capacity of stainless steel 316 | $J\,kg^{-1}\,K^{-1}$ |
| $K_{ss}$ | 16.3 | Thermal conductivity of stainless steel 316 | $W\,m^{-1}\,K^{-1}$ |
| $c_{pH_2O}$ | 75.43 | Heat capacity of water | $J\,mol^{-1}\,K^{-1}$ |
| $c_{pO_2}$ | 29.39 | Heat capacity of oxygen | $J\,mol^{-1}\,K^{-1}$ |
| $P_o$ | $1.01 \times 10^5$ | Initial pressure at inlet | Pa |
| $H$ | $1.15 \times 10^{-3}$ | Average dynamic viscosity of $H_2O_2$ solution | Pa s |

## Appendix B. Simulation scalar expressions

| Equation symbol | Expression | Description | SI units |
|---|---|---|---|
| $r_{H_2O_2}$ | $k_{rxn}C_{H_2O_2} \times M_{cat}$ | Rate law for $H_2O_2$ consumed | $mol\,m^{-3}\,s^{-1}$ |
| $r_{H_2O}$ | $-r_{H_2O_2}$ | Rate law for $H_2O$ produced | $mol\,m^{-3}\,s^{-1}$ |
| $r_{O_2}$ | $0.5(r_{H_2O})$ | Rate law for $O_2$ produced | $mol\,m^{-3}\,s^{-1}$ |
| $k_{rxn}$ | $Ae^{-E_a/RT}$ | Arrhenius reaction rate constant | $mol\,m^{-3}\,s^{-1}\,g_{cat}^{-1}$ |
| $X_{conv}$ | $(C_{H_2O_2,0} - C_{H_2O_2})/C_{H_2O_2,0}$ | Conversion | 1 |
| $C_{O_2}$ | $C_{H_2O_2,0}\left[\frac{0.5 \cdot X_{conv}}{(1+0.5 \cdot x_{H_2O_2,0} \cdot X_{conv})}\right] T_o/T$ | $O_2$ concentration | $mol\,m^{-3}$ |
| $C_{H_2O}$ | $C_{H_2O_2,0}((x_{H_2O,0}/x_{H_2O_2,0}) + X_{conv})$ | $H_2O$ concentration | $mol\,m^{-3}$ |
| $x_{H_2O_2}$ | $C_{H_2O_2}/(C_{H_2O_2} + C_{O_2} + C_{H_2O})$ | Mole fraction $H_2O_2$ | 1 |
| $x_{H_2O}$ | $C_{H_2O}/(C_{H_2O_2} + C_{O_2} + C_{H_2O})$ | Mole fraction $H_2O$ | 1 |
| $y_{O_2}$ | $C_{O_2}/(C_{H_2O_2} + C_{O_2} + C_{H_2O})$ | Mole fraction $O_2$ | 1 |
| $S_h$ | $c_{pH_2O}(373 - T_o)r_{H_2O} + c_{pO_2}(373 - T_o)r_{O_2}$ | Sensible heat | $W\,m^{-3}$ |
| $\Delta H_{vap}$ | $-49.004T + 58754$ | Heat of water vaporization | $J\,mol^{-1}$ |
| $D_{H_2O_2eff}$ | $D_{effpp}(x_{H_2O_2}) + D_{effpH_2O}(x_{H_2O})$ | Diffusion of $H_2O_2$ into solution | $m^2\,s^{-1}$ |

## Appendix C. Boundary conditions

| Boundary | Boundary condition | Equation |
|---|---|---|
| **Mass balance** | | |
| Inlet | Initial $H_2O_2$ concentration | $C = C_{H_2O_2,0}$ |
| Outlet | Convective flux; no diffusive flux | $\boldsymbol{n}(-D_{eff}\nabla C_{H_2O_2} = 0)$[a] |
| Reactor walls | Symmetry | $\boldsymbol{n}(-D_{eff}\nabla C_{H_2O_2} + C_{H_2O_2}v_x = 0)$ |
| **Energy balance** | | |
| Inlet | Initial temperature | $T = T_o$ |
| Outlet | Convective flux; no conductive flux | $\boldsymbol{n} \cdot (-K_{eff}\nabla T = 0)$ |
| Internal surfaces | Continuity | $\boldsymbol{n} \cdot (q_1 - q_2) = 0;\ q_i = -K_{effi}\nabla T_i + \rho_i c_{p_i} U_i T_i$ |
| External surfaces | Heat flux | $\boldsymbol{n} \cdot (-K_{eff}\nabla T + \rho c_p UT) = h_{conv}(T - T_{ambient})$ |
| **Momentum balance** | | |
| Inlet | Inflow velocity | $U = v_{xo}\hat{\imath}$ |
| Outlet | Normal flow/pressure | $P = P_{atm}$ |
| Reactor walls | No slip | $U = 0$ |

[a] $\boldsymbol{n}$ represents the normal outward vector.

## References

[1] United States' Department of the Navy, The Navy Unmanned Undersea Vehicle (UUV) Master Plan, 2004, http://www.navy.mil/navydata/technology/uuvmp.pdf.

[2] J.B. Lakeman, A. Rose, K.D. Pointon, D.J. Browning, K.V. Lovell, S.C. Waring, J.A. Horsfall, J. Power Sources 162 (2006) 765–772.

[3] A.A. Burke, L.G. Carreiro, J. Power Sources 158 (2006) 428–435.

[4] A.A. Burke, L.G. Carreiro, E.S. Greene, J. Power Sources 176 (2008) 299–305.

[5] C. Bramanti, A. Cervone, L. Romeo, L. Torre, L. d'Agostino, A.J. Musker, G. Saccoccia, Proceedings of 42nd AIAA/ASME/ SAE/ASEE Joint Propulsion Conference & Exhibit Sacramento, CA, USA, 2006.

[6] N.S. Davis, J.H. Keefe, Ind. Eng. Chem. 48 (4) (1956) 745–748.

[7] C. Kappenstein, et al., Appl. Catal. A 234 (2002) 145–153.

[8] M.W. Rophael, N.S. Petro, L.R. Khalil, J. Power Sources 22 (1988) 149–161.

[9] M. Deraz, H.H. Salim, A. Abd El-Aal, Mater. Lett. 53 (2002) 102–109.

[10] M.A. Hasan, M.I. Zaki, L. Pasupulety, K. Kumari, Appl. Catal. A 181 (1999) 171–179.

[11] H2O2.com. Thermodynamic Properties. http://www.h2o2.com/intro/properties/thermodynamic.html.

[12] M. Papadaki, E. Marqués-Domingo, J. Gao, T. Mahmud, J. Loss Prev. Process Ind. 18 (4-6) (2005) 384–391.

[13] J. Guo, Y. Jiang, M.H. Al-Dahhan, Chem. Eng. Sci. 63 (3) (2008) 751–764.

[14] W. Ehrfeld, V. Hessel, H. Löwe, Microreactors: New Technology for Modern Chemistry, 1st ed., Wiley–VCH, Weinheim, 2000, pp. 5–8.

[15] K.F. Jensen, Chem. Eng. Sci. 56 (2) (2001) 293–303.

[16] J. Xu, Y. Feng, J. Cen, Int. J. Heat Mass Transfer 50 (5-6) (2007) 857–871.

[17] C.E. Brennen, Fundamentals of Multiphase Flow, Cambridge University Press, New York, NY, 2005, pp. 127–133.

[18] A. Faghri, Y. Zhang, Transport Phenomena in Multiphase Systems, Academic Press, Burlington, MA, 2006.

[19] J.J. Van, Z. Laar, Phys. Chem. 72 (723) (1910).

[20] COMSOL, COMSOL News. Questions and Answers from the Support Desk, 2007, p. 17.

[21] E.B. Bird, W.E. Stewart, E.N. Lightfoot, Transport Phenomena, 2nd ed., John Wiley & Sons, Inc., New York, NY, 2002.

[22] H2O2.com. Product information: high level assay analytical method (permanganate titration). http://www.h2o2.com/intro/highrange.html.

[23] F.S. Fogler, M.N. Gürmen, Elements of Chemical Reaction Engineering, Prentice Hall, Upper Saddle River, NJ, 2005.

[24] W.C. Schumb, C.N. Satterfield, R.L. Wentworth, Hydrogen Peroxide, Chapman & Hall, University of California, Reinhold, 1955.

[25] P.L. Mills, D.J. Quiram, J.F. Ryley, Chem. Eng. Sci. 62 (2007) 6992–7010.